Surface plasmon lasers

Tenner, V.T.

Chapter 6

Two-mode surface plasmon lasing in hexagonal arrays

We demonstrate surface-plasmon lasing in hexagonal metal hole arrays with a semiconductor gain medium. The device can be tuned between two laser modes, with distinct wavelengths, spatial distributions and polarization patterns by changing the size of the optically pumped area. One of the modes exhibits a six-fold polarization pattern, while the mode observed for larger pump spots has a rotationally symmetric polarization pattern. We explain the mode tuning by the differences of in-plane and radiative out-of-plane losses of the modes. The spatial and polarization properties of the modes are conveniently described by a sum of vectorial OAM beams with orbital, spin and total angular momentum $j = \ell + s$.

6.1 Introduction

Periodic structures and crystals scatter waves and create standing waves that can completely stop the wave propagation in specific crystal directions. The absence of propagating modes has important consequences. Atoms arranged in a crystalline structure give rise to electronic bandgaps and have opened the wide field of electronics. Analogously, periodic dielectric structures [78] have stimulated developments in photonics and have enabled, among others, planar photonic crystal reflectors [108–110], compact etalon filters [111, 112], and high-performance photonic crystal lasers emitting at wavelengths ranging from the visible regime [36, 113, 114] to the THz regime [31, 32]. The revival of the field of surface plasmons (SPs) was triggered by the observation of extraordinary transmission in crystals in the form of metal hole arrays. We combine similar plasmonic crystals with gain, to compensate the intrinsic SP losses and create a SP laser.

Plasmonic crystals have different optical properties compared to photonic crystals at visible and telecom wavelengths. In plasmonic crystals, the avoided crossings in the band structure are small, often hardly resolvable and no complete band gaps are possible. This implies that the feedback needed for laser operation is low, while the losses of surface plasmons are high due to electron scattering (Ohmic loss) and hence high gain is needed in order to reach the laser threshold. The mode volume of SP lasers can be much smaller than their photonic counterpart [22] and thus the power needed to reach threshold may be lower nevertheless. We address the question to what extent the theory for photonics systems can be applied to plasmonic.

In this chapter, we demonstrate SP lasing in hexagonal plasmonic crystals. To our surprise, we find lasing in two modes with different polarization profiles. Tuning between these modes is achieved by changing the size of the pump spot. We link this observation to previous experimental and theoretical work on photonic crystals. Furthermore, we explain the mode and polarization profiles from symmetry arguments and show that a compact description of the mode profiles can be given in terms of a sum of orbital angular momentum (OAM) beams.

6.2 Setup and Methods

Our devices consist of a hole array in a 100 nm thick gold film on an InP semiconductor substrate containing a 127 nm thick $In_xGa_{1-x}As$ ($x = 0.536$) gain layer. Holes with a diameter of 160 nm are placed in a hexagonal lattice with hole spacing $a = 525$ nm. This sample is manufactured using the same procedure on the same wafer as the samples in ref. [95].

Our experimental geometry is as follows: the sample is optically pumped at normal incidence on the semiconductor side with a Gaussian beam from a continuous-wave laser with a wavelength of 1064 nm. Light is collected on the other side of the sample and analyzed with a CCD camera. The SP-laser light is selected with a 12 nm wide band-pass filter centered around the wavelength of

the lasing SP-mode. Polarization-resolved (stokes parameters) and phase-resolved measurements of the optical field are performed in the far- and near- field of the laser beam. The dispersion of the SP modes on the hole array are measured by recording the emission spectrum $I(\omega, \boldsymbol{\theta})$ as function of angle $\boldsymbol{\theta} = (\theta_x, \theta_y)$ to find the relation $\omega(\boldsymbol{k}_{\mathrm{sp}})$, where $\boldsymbol{k}_{\mathrm{sp}} = \boldsymbol{k}_{\parallel,\mathrm{photon}}$ (modulo the lattice vectors) and $\left|\boldsymbol{k}_{\parallel,\mathrm{photon}}\right| = (\omega/c)\sin|\boldsymbol{\theta}|$ [37, 95]. This experimental geometry is described in more detail in ref. [37, 65].

6.3 Results

We observe SP lasing in two distinct modes, which emit at wavelengths $\lambda \approx 1470$ nm and $\lambda \approx 1500$ nm. We attribute the high-energy mode to the A-band of the dispersion relation [95] and the low-energy mode to the B-mode. The A-band is known to have a monopole-like charge distribution [98, 115] and is expected to radiate radially polarized light [115]. The B-mode has a hexapole-like charge distribution and therefore is expected to have a more complex polarization pattern.

Figures 6.1(a) and (b) show images of the sample plane, i.e. they show the radiative part of the near-field of the SP-laser mode. The A-mode is donut shaped; it has a dark center with a bright ring around it. The B-mode has a different profile; it has six bright lobes placed in a hexagonal shape. Another striking difference is the size of the modes. The A-beam shown in Fig. 6.1 has a max-max diameter of 22.4(5) μm and the B-mode has a diameter of 10.2(4) μm. The images in Fig. 6.1 are obtained with a slightly elliptical Gaussian pump spot with an average full-width-half-max (FWHM) diameter of 15.9 ± 0.7 μm and 7.2 ± 0.7 μm for respectively the A- and B-mode. The ±0.7 μm indicates the difference between the long (short) axis and the average diameter. The diameter of the laser area changes when we change the size of the pump spot. The A-mode is always larger than the B-mode in our device.

Figure 6.1 also shows the polarization state of the light. The measured Stokes parameters are visualized as white ellipses. The A-mode is mainly radially polarized; only the areas with high intensity show some elliptically polarized light (Stokes parameter $s_3 < 0.7$). The polarization of the monopole A-mode resembles the sum of two orbital-angular-momentum (OAM) beams with total angular momentum $j = \ell + s = 0$ ($\ell = \mp 1, s = \pm 1$) [116–120], as illustrated in the inset of Fig. 6.1(a) and discussed below. The polarization of the hexapole B-mode has a mixed radial and azimuthal character. The polarization changes six times from radial to azimuthal over the full 2π angular range, i.e. it resembles a $j = \pm 3$ ($\ell = \pm 2, s = \pm 1$) beam. The OAM description also includes the relative phase of different parts of the beam, which is indicated by the direction of the arrows in the insets of Fig. 6.1. This information cannot be derived from the Stokes parameters. It was obtained in a phase-resolving experiment with the technique described in ref. [65], which yields the local field polarization and phase as shown in Appendix 6.A. We thus confirmed that the polarization-arrows are in the directions indicated in the insets

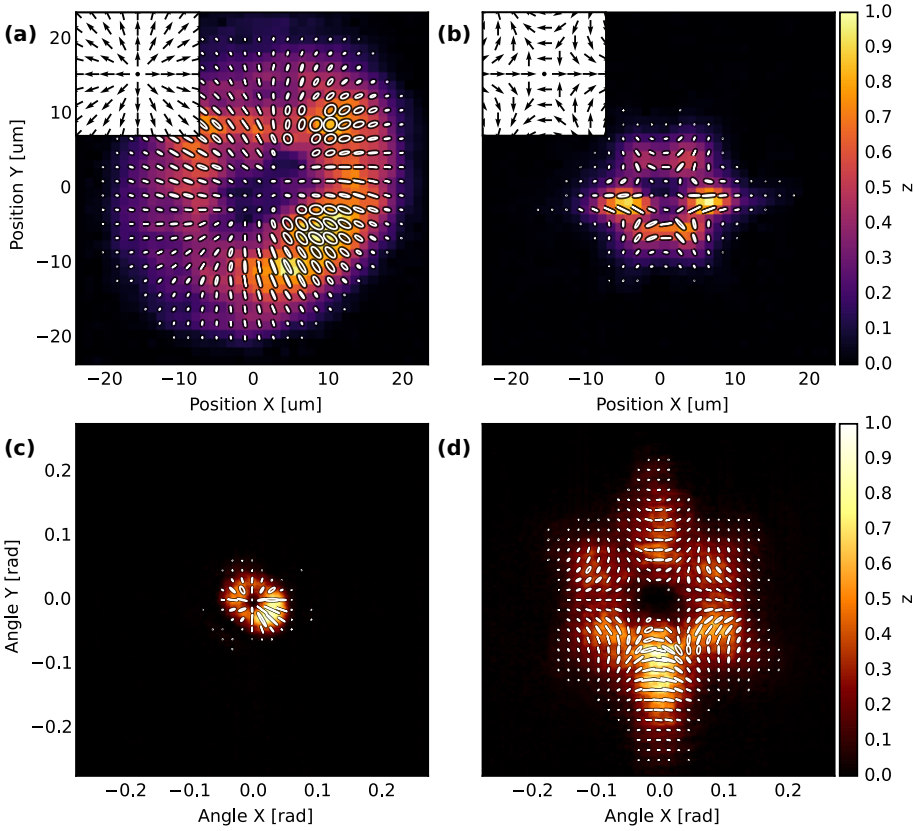

Figure 6.1: Intensity and polarization profiles of a surface plasmon laser in a hexagonal lattice under excitation with a pump spot of (a, c) ~ 16 µm diameter or (b, d) ~ 7 µm diameter. The monopole A-mode has (a) a large lasing area, and (c) a compact far-field. The hexapole B-mode has (b) a small lasing area, and (d) a wide far-field. The white ellipses indicate the local polarization direction and state of the light. Insets: Polarization pattern of a sum of OAM modes with (a) $j = 0$ for the A-mode, and (b) $j = \pm 3$ for the B-mode.

of Fig. 6.1(a,c).

The measured local phase of the beams also contains additional information: it shows that the A-mode has a positive radial phase-gradient. A similar gradient is observed for the A-mode in square-lattices [65]. The B-mode has a negative radial phase-gradient. These signs are as expected: the sign of the phase gradient depends on the operation wavelength compared to the lattice spacing, and a wavelength $\lambda > \sqrt{3} n_{eff} a/2$ will induce a negative phase-gradient, as is the case for the low-energy B-mode

Figures 6.1(c, d) show the far-field beam profiles. They are comparable to the near-field beam profiles described above: the A-mode is again donut-shaped, while the B-mode is hexagonal shaped. The difference is the opening angle; the large area of the A-mode generates a compact far-field with a max-max openings angle $2\Delta\theta = 56(4)$ mrad, while the small area of the B-mode generates a wide far-field with opening angle $2\Delta\theta = 162(10)$ mrad. The etendue $G = (\pi \Delta r \Delta\theta)^2$ is 1.0 μm^2 for the A-mode and 1.7 μm^2 for the B-mode. Furthermore, the six-lobed far-field intensity distribution of the B-mode is rotated by 90° compared to its near-field, while the polarization profile is not rotated.

The laser threshold and input-output characteristics of both modes are different. The A-mode has a threshold of 150(10) mW and an input-output slope $dP_{\text{out}}/dP_{\text{in}} = 5.2(5)$ μW/mW, while the B mode has a higher threshold of 200(3) mW and a steeper slope of 15(1) μW/mW for the pump sizes mentioned above. The larger slope indicates that the B-mode radiates more efficiently. The threshold and slope depend on the location on the sample and on the pump spot size. The observed thresholds are typically within 50 mW of the thresholds mentioned above. The laser threshold of the A-mode is typically higher than that of the B-mode. More details are shown in Appendix 6.B.

The A- and B-mode lase under distinct conditions. The A-mode lases when a large area is pumped, while the B-mode lases when a smaller area is pumped. The pump spot diameter at which the laser switches is typically 15 ± 1 μm for a pump power of 250 mW. Hence we can select a laser mode by tuning the size of the pumped area.

We studied the existence of the A- and B- laser mode in samples similar to the one described above and observed laser action in monopole and hexapole modes in samples with minimum hole spacing of $a = 515$, 525, and 535 nm. Besides samples with a hexagonal lattice, we also studied metal hole array lasers with honeycomb and kagome lattices. All observed laser beams are similar to the results reported here. Also in these lattices the desired laser mode can be selected by tuning the size of the pumped area. From this we conclude that lasing in two modes is a universal property of hexagonal-based (C_{6v} point group) lattices.

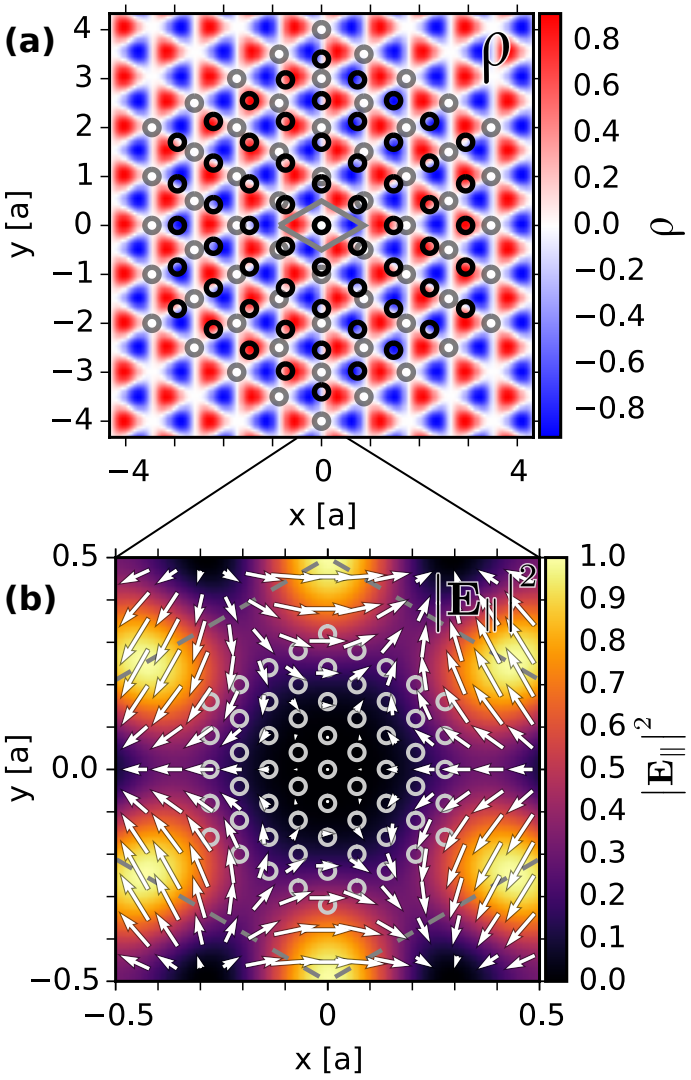

Figure 6.2: Model to understand radiation and polarization of a mode near the Γ-point, applied to the B-mode. (a) The charge distribution ρ of 9×9 unit cells. The grey rhombus indicates a single unit cell. The grey circles indicate the position of the holes when the lattice- and wave-vector are identical. The black circles indicate the (exaggerated) position of the holes for a wave-vector that is slightly shorter than the lattice-vector. (b) The black holes have been folded back on the unit cell. The polarization and intensity of the in-plane field $\mathbf{E}_{\parallel}$ is indicated with respectively white arrows and the colored background.

6.4 Discussion

The distinct profiles and polarizations of the A- and B-mode follow from symmetry by a two-step argument. First, the symmetry of the unit cell and lattice together dictate the charge distribution ρ [34, 98], and thereby the out-of-plane field $E_\perp \sim \rho$ [98] and the in-plane field $\mathbf{E}_\parallel \sim \boldsymbol{\nabla} \mathrm{E}_\perp$. For modes at the Γ-point ($k = 0$), the charge distribution can be described by an irreducible representation of the C_{6v} point group. Radiation to free space is governed by the in-plane H-field $\mathbf{H}_\parallel$ [37, 115], associated with the in-plane E-field $\mathbf{E}_\parallel$. Second, the radiation profile of the full device resembles the field distribution inside a single unit cell. This argument applies because the laser operates close to the Γ-point ($k \neq 0$) and is based on translation symmetry (Bloch theorem) and "spatial sampling" as explained below.

To elucidate the second step, we focus on the hexapole B-mode. Figure 6.2(a) shows the charge distribution of the hexapole B-mode [98]. The grey circles indicate the position of the holes when the lattice and wave vector are identical ($k = 0$), i.e. the lattice spacing is $a = 2\lambda_{sp}/\sqrt{3}$. Because SP lasers do not operate exactly at the Γ-point, but close to it [35, 65], the wave vectors are slightly longer or shorter than the lattice vector ($k \neq 0$). In our perturbative approach we neglect the influence of the holes on the fields. In this approach the mismatch $k \neq 0$ merely results in an elongation or contraction of the full field pattern relative to the lattice and therefore the nodes of the fields do not align with the position of the holes. This is illustrated in Fig 6.2(a), where the black circles indicate the (exaggerated) position of the holes for a wave vector that is slightly shorter than the lattice vector. Translation symmetry of the field pattern and the lattice now allows one to fold back the position of the (shifted) holes on the unit-cell [121, 122]. Every hole thereby samples the field at a different location in the unit cell as is indicated in Fig. 6.2(b). Hence, with this second, "spatial sampling", step we have mapped the radiated near-field of the whole lattice to the field inside a single unit cell. Figure 6.2(b) shows the predicted intensity and polarization of the radiating field for the B-mode; these patterns indeed resemble the experimentally observed polarization.

More quantitative results can be derived by Taylor-expanding the radiating field around the central hole in the unit cell. We performed this Taylor expansion for the radiating field derived from the charge distribution presented in ref. [98]. The resulting expression can be written as the sum of two $\pm j$-OAM beams; for the A-mode $j = 0$ ($\ell = \mp 1$, $s = \pm 1$) and for the B-mode $j = \pm 3$ ($\ell = \pm 2$, $s = \pm 1$). This is consistent with the observed polarization patterns in Fig. 6.1.

The experimentally observed polarization patterns can be described by the sum of two orbital angular momentum (OAM) beams with opposite circular polarization [116–120]:

$$\mathbf{E}^\ell(r, \phi) = u(r)\left[\exp\left[-i(\ell\phi + \varphi)\right]\mathbf{e}_+ + \exp\left[i(\ell\phi - \varphi)\right]\mathbf{e}_-\right] \tag{6.4.1}$$

where (r, ϕ) are the radial and azimuthal coordinate of the beam. This function is the superposition of two components with helicity $s = \pm 1$ and orbital angular momentum $\mp\ell$. Equation (6.4.1) describes a field that has uniform intensity around the ring (azimuthal direction) and has a linear polarization everywhere. The phase difference 2φ between both polarizations determines the local orientation of the polarization. For example, $\ell = \mp 1$ describes a radial polarization when $\varphi = 0$, while it describes an azimuthal polarization when $\varphi = \pi/2$.

The radial part of the beams can be described with a $p = 0$ Laguerre-Gauss amplitude function $u(r) \propto r^{|\ell|} \exp\left(-r^2/r_0^2\right)$. The etendue of such Laguerre-Gauss OAM modes scales as $G \propto (2p+|\ell|+1)^2$ [120, 123], making $G_A/G_B = \left(\frac{|\ell=\mp 1|+1}{|\ell=\pm 2|+1}\right)^2 = 0.44$. This is in reasonable agreement with the experimental observed etendue $G_A/G_B = 0.56$. OAM beams are an effective description of the observed modes. They describe both the polarization pattern and the etendue.

There are two experimental observations that require us to go beyond the description presented in Eq. (6.4.1) and consider more than two OAM beams. First, the six bright lobes in the intensity profile of the B-mode indicate that this is not a pure $\pm j$ mode; these lobes can be explained by a mixture of 90% $j = \pm 3$ ($\ell = \pm 2$, $s = \pm 1$) and 10% of a $j = \mp 3$ ($\ell = \mp 4$, $s = \pm 1$) mode. Second, the A- and B-mode have distinct azimuthal profiles, while their radial profiles have approximately the same shape $u(r) \sim r^\beta \exp\left(-r^2/r_0^2\right)$ with $\beta \simeq 1$ (see Appendix 6.A). This profile is expected for the A-mode ($|\ell| = 1$), but strange for the B-mode ($|\ell| = 2$). Phenomenologically, we can explain the strange radial profile by admixing modes with a $p \neq 0$ component. However, the underlying physics is not yet understood. It might be related to the unbalance between the traveling waves that builds up outside the center of the device by the combined action of gain and feedback [35]. This unbalance removes the field nodes, enables radiation [87], and modifies the emitted intensity profile [72].

We can tune which mode lases by changing the pump spot size. To explain this behavior, we will discuss the total loss of both modes, and distinguish between in out-of-plane and in-plane loss.

The out-of-plane loss is radiative loss; it depends on the laser area, the spatial distribution of the modes, the scattering properties of the holes [52], the wave vector detuning [87], and the refractive index profile [65]. The radiative loss of the hexapole B-mode is higher than the monopole A-mode, as indicated by the higher slope of the threshold measurements. This is consistent with the field distribution picture presented above: the hexapole has more structure and its field increases more rapidly around the central hole in the unit cell than the monopole field. Hence the hexapole mode will radiate more efficiently at holes outside the center of the device.

The in-plane loss results from SPs that leave the pumped area due to insufficient feedback. The magnitude of the total in-plane loss depends on the length of the boundary of the pumped area. The feedback depends on the product of the effective

in-plane coupling κ and the device length L [35]. The effective in-plane coupling coefficient κ contains contributions from scattering of all traveling waves and can thus be different for both modes [124]. We speculate that the effective in-plane coupling constant κ_A of the A-mode is smaller than κ_B of the B-mode, such that the A-mode requires a larger pump spot to obtain the same κL product.

We can tune the ratio between in-plane (circumference) and out-of-plane (surface) loss by changing the size of the pumped area; when the pumped area is small the ratio between circumference and surface is large. Hence lasing is favored in the B-mode with a low in-plane loss (high feedback), while a higher surface loss can be tolerated. When the pumped area is large, the device prefers to operate in a mode with less surface loss, while a high in-plane loss (limited feedback) can be tolerated and hence the device lasers in the A-mode.

Finally, we compare our observation of monopole and hexapole laser modes to previous results on photonic crystals. Imada *et al.* [72] reported on the hexapole mode in photonic crystals, for modes with a transverse electric (TE) polarization. In those electrically pumped experiments, an electrode was obscuring the view on the radiated light. The observed polarization is rotated 90° compared to our TM-modes. Liang *et al.* [124] demonstrated tuning between the monopole and hexapole mode by changing the size of the holes in a dielectric slab and hence changing the in-plane losses. The monopole and hexapole modes are also observed in the THz regime for modes with TM-polarization [115]; the polarization of the far field is observed, and selection between the modes is obtained by tuning a narrow-band gain spectrum to the resonance frequencies of the modes. From this we conclude that lasing in two modes is a universal property of hexagonal-based (C_{6v} point group) lattices.

6.5 Conclusion

In conclusion, we have observed SP-lasing in hexagonal metal hole arrays, both in a monopole and in a hexapole mode. The modes have different spatial and angular profiles which all resemble a superposition of circularly polarized OAM beams: a monopole mode with total angular momentum $j = 0$ ($\ell = \mp 1$, $s = \pm 1$), and a hexapole mode with $j = \pm 3$ ($\ell = \pm 2$, $s = \pm 1$). The observed intensity and polarization profile can be explained by symmetry arguments. Mode selection can be achieved by tuning the size of the pump spot, which affects the ratio between in-plane and out-of plane loss. These observations in TM-polarized plasmonic lasers are consistent with previous work on TE-polarized photonic crystals.

Acknowledgment. The authors thank Eric R. Eliel for useful discussions and feedback, and Peter J. van Veldhoven and Erik Jan Geluk for their help in fabricating the samples at the COBRA Research Institute of the Technische Universiteit Eindhoven, The Netherlands.

Appendices

In these appendices, we present the vectorial E-field of SP lasers in hexagonal arrays. The polarization of the field is explicitly presented as Stokes parameters, while it is implicit in the combined intensity and phase plots. Furthermore, we show the peculiar behavior of the SP lasers around laser threshold.

6.A Polarization, intensity and phase

We first give a Stokes representation of the polarization state of the emitted laser light. The s_0 parameter indicates the intensity of the light, the s_1 and s_2 parameters indicate the linear polarized state of light in two different polarization bases, and the s_3 parameter indicates the circular polarization state. The Stokes parametes s_1 and s_2 are measured by projecting the laser on a linear polarizer at four different orientations $(-45°, 0°, 45°, 90°)$ and the circular Stokes parameter s_3 is measured with an additional quarter-wave plate.

Figure 6.3 shows the measured Stokes parameters of the far-field beam profiles of the A- and B- mode. Measurements of s_1 and s_2 on the A-mode yield two-fold symmetric patterns as expected for a $\ell = \mp 1$ beam. The A-mode is predominantly radially polarized. The light is in a linearly polarized state along the $\theta_x = 0$ and $\theta_y = 0$ axis, while it is slightly elliptically polarized, with circular Stokes parameter $|s_3| < 0.7$, in the 45° direction. While symmetry prohibits emission of elliptically polarized light along mirror planes of the lattice, it does not prohibit emission of elliptically polarized light in other directions. The s_1 and s_2 parameters of the B-mode show a four-fold symmetric pattern, as expected for a $\ell = \pm 2$ beam. The B-mode polarization is six-fold azimuthally and radially polarized; it is azimuthally polarized in the Γ-K directions of the lattice and radially polarized in the Γ-M directions.

We have measured intensity and retrieved phase with a technique described in chapter 4. Figure 6.4 shows the measured intensity and retrieved phase of the A- and B-mode measured behind a horizontal (top row) or vertical (bottom row) polarizer. The polarization-resolved intensity measurements in Figs. 6.4(a, b) and Figs. 6.4(e, f) contain equivalent information as the Stokes s_1 parameter, which is already discussed above. Now we will discuss the phase profiles of the beams, which contain additional information. Figures 6.4(c, d) show the retrieved phase profile of the A-mode. The sharp transition in the dark center indicates a π-phase jump. This show that the electric fields on opposite sides of the beam are pointing in opposite directions, as expected for radially polarized light. Furthermore, the phase has a positive radial gradient; the phase increases by 0.5(2) rad from the center to the edge of the laser area. Figures 6.4(g, h) shows that the phase of the B-mode has a more complex profile; in both polarizations it is four-lobed. The phase of neighboring lobes is shifted by π-phase jump. The phase gradient of this mode is negative; the phase decreases by 0.7(3) rad from the center to the edge of the laser area.

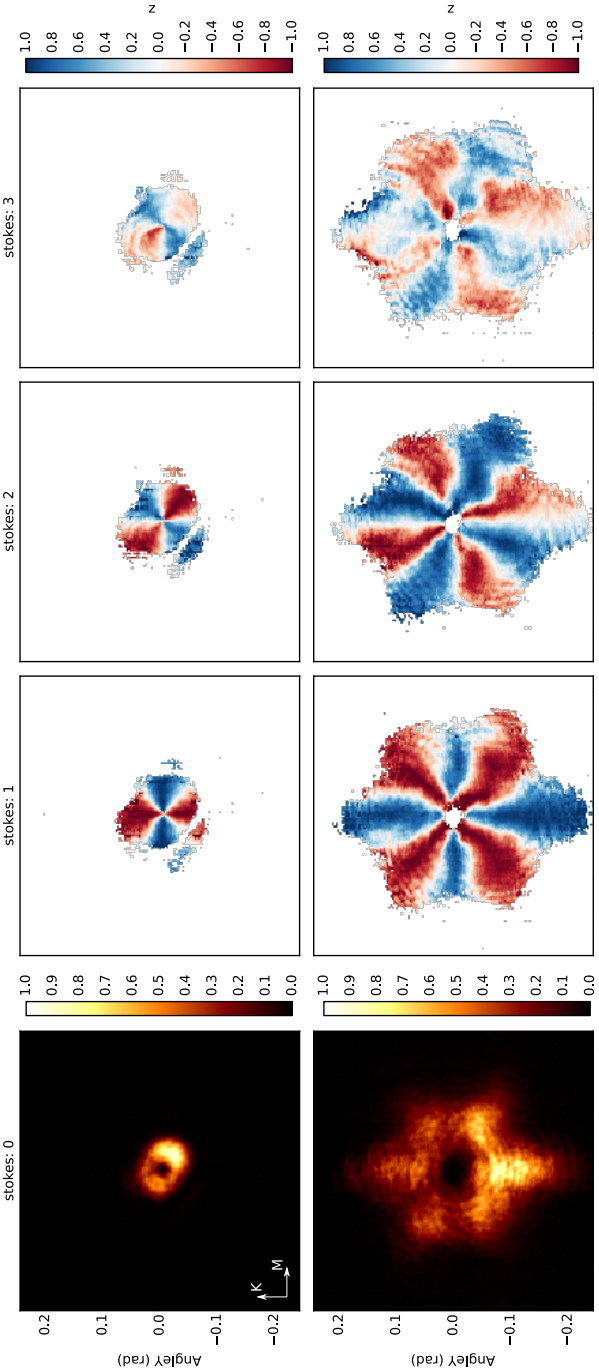

Figure 6.3: Stokes parameter representation of the far-field of the (top row) A- and (bottom row) B-mode.

Figure 6.4: Polarization resolved intensity and phase of the (a-d) A- and (e-h) B-mode. (a, b, e, f) Near field intensity and (c, d, g, h) phase distribution, measured behind a horizontal (top row) or vertical (bottom row) polarizer. Note that the phase is only shown from areas with sufficient intensity, i.e. more than 3% of the maximum intensity.

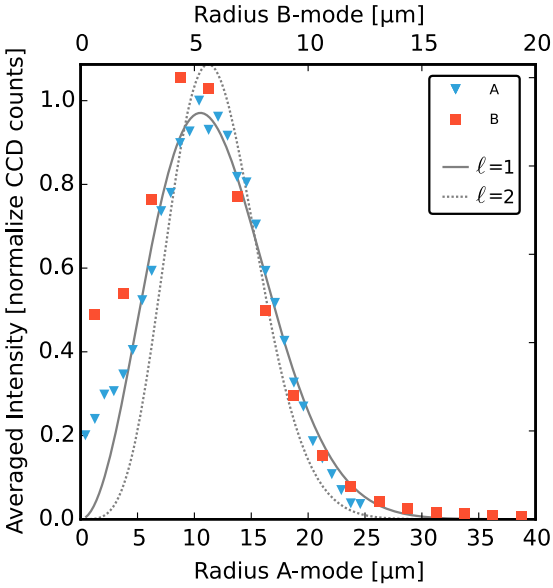

Figure 6.5: Radial intensity profile of the A- and B-modes. The curves indicate fits with Laguerre-Gauss modes with different ℓ.

The reported phase gradients originates from the mismatch between the wave-vector and the lattice-vector: a negative phase gradient is obtained when the SP wave-vector is shorter than the lattice-vector, such that the field at holes more outwards from the center lags behind the field at the center (see Fig. 6.2 for an illustration), and vice versa. The magnitude of the phase gradient can be modified by a non-uniform refractive index profile [65].

Figure 6.5 shows the measured radial intensity-profile of the A- and B-mode. The rotationally-averaged intensity is normalized by its maximum value. The radial intensity profiles of both modes are surprisingly similar. These profiles are fitted with $I(r) = |u(r)|^2$ where $u(r) \sim r^\beta \exp\left(-r^2/r_0^2\right)$; the resulting curves for $\beta = 1$ and $\beta = 2$ are displayed in Fig. 6.5 with respectively a solid and a dashed curve. The best overlap is found for $\beta = 1$ and the obtained beam widths are reported in section 6.3. An analysis of the beam profiles in the far-field shows that the radial profiles of the beams have the same shape and can also be best described by $\beta = 1$ (data not shown).

6.B Laser threshold

Figure 6.6 shows the power of the SP laser as a function of the pump power for lasing in the A- and B-mode. The output of the B-mode exhibits a clear threshold around 200 mW and increases linearly above threshold with slope

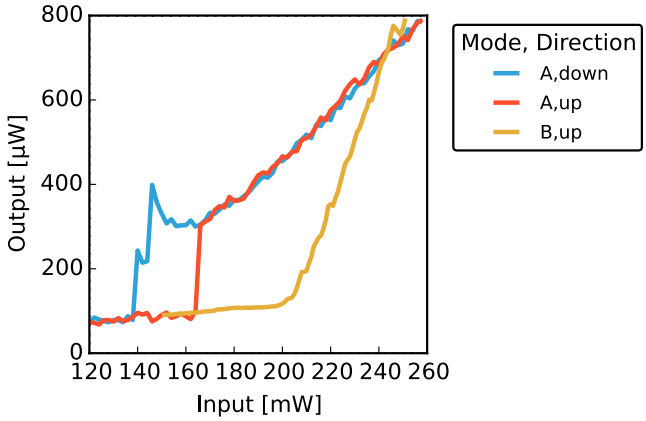

Figure 6.6: The output power of the SP lasers as a function of the pump power for lasing in the A- and B-mode.

$dP_{\mathrm{out}}/dP_{\mathrm{in}} = 15(1)\,\mu\mathrm{W/mW}$ and does not show hysteresis. The A-mode has a more complicated input-output behavior. When scanning the input power from 100 mW up to 260 mW, the mode suddenly starts to laser in a step-wise fashion at threshold power $P_{\mathrm{up}} = 160(2)\,\mathrm{mW}$ and increases in power with a smaller slope $dP_{\mathrm{out}}/dP_{\mathrm{in}} = 5.2(2)\,\mu\mathrm{W/mW}$. The A-mode shows hysteresis: when decreasing the power below P_{up}, the laser stays active till the threshold $P_{\mathrm{down}} = 140(2)\,\mathrm{mW}$. Even more surprising is that the output power increases just above the threshold P_{down} upon reduction of the pump power. We attribute this hysteresis to heating of the sample.